UC Berkeley
UC Berkeley Previously Published Works

Title

Systematic investigation of composition—microstructure—property relationships in the HCP Ti-Zr-Hf model system

Permalink

https://escholarship.org/uc/item/4sb335vr

Journal

Acta Materialia, 321

ISSN

1359-6454

Authors

Yoon, Kooknoh
Lyu, Haomin
Chen, Xiaoyu
et al.

Publication Date

2026-12-01

DOI

10.1016/j.actamat.2026.122719

Copyright Information

This work is made available under the terms of a Creative Commons Attribution License, available at https://creativecommons.org/licenses/by/4.0/

Peer reviewed

eScholarship.org Powered by the California Digital Library
University of California

Acta Materialia 321 (2026) 122719

Contents lists available at ScienceDirect

Acta Materialia

journal homepage: www.elsevier.com/locate/actamat

Systematic investigation of composition–microstructure–property relationships in the HCP Ti-Zr-Hf model system

Kooknoh Yoon [a,d,*], Haomin Lyu [b,c], Xiaoyu Chen [b,c], Andrew M. Minor [b,c], Mark Asta [b,c], Daryl Chrzan [b], Peter Hosemann [a,b,*]

[a] Department of Nuclear Engineering, University of California, Berkeley, CA, USA
[b] Department of Materials Science and Engineering, University of California, Berkeley, CA, USA
[c] National Center for Electron Microscopy, Molecular Foundry, Lawrence Berkeley National Laboratory, Berkeley, CA, USA
[d] Department of Materials Science and Engineering, Hanbat National University, Yuseong-gu, Daejeon, 34158, Republic of Korea

ARTICLE INFO

Keywords:
High entropy alloys
HCP alloys
Solidifications
CCT diagram
Deformation mechanism

ABSTRACT

Hexagonal Close-Packed (HCP) alloys are used in structural materials applications for extreme environments such as those involving cryogenic conditions, or for nuclear cladding. However, the alloy design space explored for HCP compositionally complex alloys, namely High-Entropy or Medium-Entropy Alloys (hereafter referred to as HEAs) has been limited. Here, we propose the Ti-Zr-Hf ternary system as an ideal model for developing single-phase HCP HEAs and systematically investigate its composition-microstructure-property relationships. CALPHAD thermodynamic calculations predicted, and experimental results confirmed, that a stable single-phase HCP solid solution forms over a wide compositional range. The as-cast microstructure exhibited a systematic evolution dictated primarily by Hf content: high-Hf content alloys formed coarse dendritic structures via diffusion-dominant transformations, whereas low-Hf alloys formed fine acicular structures through diffusionless martensitic transformations. This change with Hf content is rationalized by a compositional dependence of the Continuous Cooling Transformation (CCT) kinetics. Nanoindentation revealed a strong solid-solution strengthening effect, with hardness generally increasing from 4.3 GPa in Ti-rich compositions to 5.5 GPa in high Hf-content alloys. Notably, the equiatomic TiZrHf alloy demonstrated an exceptional synergy of high yield strength (1140 MPa) and superior ductility (elongation >16%). Post-deformation analysis revealed that this is governed by the Twinning-Induced Plasticity (TWIP) effect, via the activation of {10-12} extension twins, confirmed by a characteristic misorientation angle of ~86° across twin boundaries. Comparing alloys of contrasting c/a ratio at fixed Ti content further revealed a transition from twinning- and stacking-fault-mediated plasticity to confined planar slip, consistent with the reduced {10-12} twinning shear and enhanced slip accessibility that accompany a higher c/a ratio; the as-cast morphology, by contrast, modulates the magnitude of the work-hardening response rather than the operative deformation mode. This work establishes the Ti-Zr-Hf system as a cornerstone for developing high-performance HCP HEAs.

1. Introduction

Conventional alloys with a Hexagonal Close-Packed (HCP) structure represent a unique class of structural materials, distinguished from cubic crystal systems like Face-Centered Cubic (FCC) or Body-Centered Cubic (BCC) by their reduced crystallographic symmetry [1–3]. This reduced symmetry leads to a significantly reduced number of possible slip systems during plastic deformation and therefore to less ductility than FCC or BCC counterparts. However, HCP materials are often selected for critical structural applications due to their capacity for high work-hardening rates and excellent specific strength, achieved through the activation of deformation twinning, or even their neutronic properties (zr-cladding) [4,5]. The fact that HCP materials retain a reasonable amount of ductility while experiencing high strength is attributed to the dynamic Hall-Petch effect [6] or twinning behavior [7,8]. Such properties are particularly crucial for addressing the challenge of low-temperature brittleness in cryogenic environments. In these conditions, where many materials exhibit a sharp decline in fracture

* Corresponding authors.
E-mail addresses: kyoon@hanbat.ac.kr (K. Yoon), peterh@berkeley.edu (P. Hosemann).

https://doi.org/10.1016/j.actamat.2026.122719
Received 18 February 2026; Received in revised form 11 August 2026; Accepted 30 August 2026
Available online 31 August 2026
1359-6454/© 2026 The Authors. Published by Elsevier Inc. on behalf of Acta Materialia Inc. This is an open access article under the CC BY license (http://creativecommons.org/licenses/by/4.0/).

toughness, the unique deformation behavior of HCP structures offers a promising foundation for developing new high-performance cryogenic materials [9,10]

High-Entropy Alloys (HEA) formed by mixing multiple principal elements in near-equiatomic ratios to create a single-phase solid solution [10–13] can reach solid-solution strengthening unattainable in conventional alloys, primarily through severe local lattice distortion, which leads to significant enhancements in mechanical properties like strength and wear resistance. This lattice distortion arises from the significant differences in atomic radii among the constituent elements and is further influenced by local variations in electronic structure and bonding, which are related to their electronegativity differences [14,15].

To date, HEA research has predominantly focused on FCC systems, exemplified by the Cantor alloy (CrMnFeCoNi), and BCC-based refractory HEAs pioneered by Senkov and others [16,17]. FCC HEAs have garnered significant attention for their remarkable fracture toughness at cryogenic temperatures [18,19], *while BCC HEAs have demonstrated exceptional strength retention in ultra-high-temperature environments; more recently, the quantitative relationship between phase constitution and the operative deformation mechanisms in these classical systems has been examined in detail by Wang et al [20]. In contrast, research on HEAs with an HCP structure remains in its nascent stages. The few reported HCP HEAs have often been designed for specific functional applications and frequently incorporate rare-earth elements, limiting their exploration as general-purpose structural materials. Rare-earth-based alloys such as Ho-Dy-Y-Gd-Tb and GdHoLaTbY have been shown to form a single-phase HCP solid solution [21–24] and to accommodate plasticity predominantly through deformation twinning and stacking faults [25]; their practical utility as structural materials is nonetheless fundamentally constrained by the high cost and limited availability of rare-earth elements, as well as their susceptibility to oxidation. Refractory systems incorporating BCC-stabilizing elements such as Nb and Ta (e.g., Ti-Zr-Hf-Nb-Ta) have also been explored, but the addition of these elements inevitably drives the phase constitution toward a BCC solid solution, making it difficult to achieve and maintain a phase-pure HCP microstructure across a broad compositional space [26,27]. Moreover, while TiZrHfNb-based refractory HEAs retain useful tensile ductility, they are characterized by comparatively low yield strength, and considerable effort has been directed at recovering strength in these alloys through interstitial and local chemical order engineering [28]. In this context, the Ti-Zr-Hf ternary system—composed exclusively of Group 4 elements that are inherently HCP-stabilizing at room temperature—offers a uniquely systematic and phase-stable platform for investigating HCP HEA behavior, clearly distinguishing it from these prior approaches.* The slower development of HCP HEAs stems from intrinsic metallurgical challenges associated with key HCP-forming elements, particularly Mg and Ti. Mg exhibits a large negative heat of mixing (ΔHmix) with most transition metals, leading to a strong tendency to form brittle intermetallic compounds rather than a stable single-phase solid solution. This thermodynamic constraint leads to the fact that Mg-based alloys (e.g., AZ31, WE43) are limited to dilute concentrations of alloying elements, fundamentally hindering the formation of an HEA single-phase solid solution [29–31]. Ti also presents difficulties, as it undergoes an allotropic transformation between the HCP (α) and BCC (β) phases and readily forms intermetallics with certain elements, making the stabilization of a single-phase HCP structure challenging [32,33].

To overcome these challenges and establish a systematic foundation for HCP HEA research, this study focuses on a model system based on the Group 4 elements: Ti, Zr, and Hf. These three elements are chemically homologous and form a continuous solid solution (isomorphous system), making them an ideal combination for creating a stable single-phase HCP structure without complex phase transformations or compound formation [34–36]. At the same time, the significant differences in their atomic radii—Ti (147 pm), Zr (160 pm), and Hf (159 pm)—offer the potential to induce severe lattice distortion when alloyed at high concentrations. This is expected to maximize the core strengthening mechanism of HEAs: solid-solution strengthening [37,38]. Accordingly, this study involves the fabrication of alloys with systematically varied compositions within the Ti-Zr-Hf ternary system via arc melting. We investigate the phase formation behavior and microstructure of these as-cast alloys and correlate these findings with their mechanical properties, ranging from the composition-dependent hardness to the tensile deformation behavior and its underlying mechanisms. Through this approach, we aim to establish the Ti-Zr-Hf system as a phase-pure HCP platform for the systematic study of HCP HEAs, and to elucidate the structure-dependent deformation mechanisms—including the activation of deformation twinning—that govern the mechanical performance of this underexplored alloy class.

2. Experimental

2.1. Thermodynamic simulations and thermal property measurements

The characteristic temperatures and thermodynamic stability of each alloy were assessed based on Calphad simulation. Particularly, ternary and vertical sections were generated using Thermo-Calc software (TCHEA3 database) to provide insights into the alloy's behavior and composition.

The phase transformation temperatures were investigated using a Linseis DIL L75 dilatometer. Specimens were heated and cooled at a constant rate of 10 K/min under a high-purity argon atmosphere to determine the α↔β transformation temperatures from the change in the coefficient of thermal expansion (CTE).

2.2. Alloy fabrications and sample preparation

A series of Ti-Zr-Hf ternary alloys were synthesized using a vacuum arc-melter. High-purity raw materials (Ti, Zr, Hf > 99.9 wt.%) were weighed to achieve the target compositions and melted under a high-purity argon atmosphere. To ensure chemical homogeneity, each button-shaped ingot was flipped and re-melted at least five times. The final ingots were cast into a water-cooled copper mold. For subsequent characterization, specimens were machined from the as-cast ingots using a precision high-speed diamond saw. The sectioned surfaces were prepared using standard metallographic procedures, involving grinding with successive SiC papers up to 2000 grit, followed by final polishing with a 0.05 μm colloidal silica suspension.

2.3. Microstructure characterization

The crystal structures of the alloys were identified using a MiniFlex 6G Benchtop X-ray Diffraction System with Cu Kα radiation. The XRD patterns were collected over a 2θ range of 20° to 100° with a 0.01° step size. The lattice parameters a and c of the HCP phase were determined from the 2θ positions of the diffraction peaks using the Bragg's law and the interplanar spacing equation for HCP structures (in 3 index Miller notation):

$$\frac{1}{d_{hkl}^2} = \frac{4}{3}\left(\frac{h^2 + hk + k^2}{a^2}\right) + \frac{l^2}{c^2}$$

where d_{hkl} is the spacing between the (hkl) planes. The c/a ratio was then calculated from these lattice parameters.

Microstructural and compositional analyses were performed using a Thermo Fisher Quattro II Scanning Electron Microscope (SEM) equipped with an energy-dispersive X-ray spectroscopy (EDS) detector. Micrographs were primarily obtained using a backscattered electron (BSE) detector to reveal compositional contrast. Crystallographic information, including phase orientation and misorientation analysis, was obtained using an Oxford Symmetry S3 electron backscatter diffraction (EBSD) detector.

2.4. Mechanical testing

The hardness and reduced elastic modulus of the materials were measured via nanoindentation (Hysitron TI 990 TriboIndenter) using a Berkovich indenter tip. Mechanical property maps were generated using the Express Test (XPM) mode. To ensure statistical reliability, indentations were arranged in an array of at least 15 × 15 with a 10 μm spacing, resulting in a minimum of 225 data points per sample.

Meso-scale tensile tests were performed on the representative equiatomic $Ti_{33.3}Zr_{33.3}Hf_{33.3}$ alloy. Tensile specimens with an 80 μm gauge width and 233 μm length were fabricated from a 100 μm thick foil sectioned from the as-cast ingot. The 'dogbone' geometries were machined using a femtosecond (fs) laser. The tests were conducted at room temperature in a Kammrath-Weiss tension module under displacement control at a strain rate of 10^{-3} s^{-1}. Digital Image Correlation (DIC) was used to accurately measure the local strain on the specimen's gauge section and correct for machine compliance.

3. Results

3.1. Thermodynamic phase stability analysis of the Ti-Zr-Hf ternary system

To establish a thermodynamic foundation for the design of a novel HCP HEA, the phase formation behavior within the proposed Ti-Zr-Hf system was investigated. Ti, Zr, and Hf are homologous elements from Group 4 of the periodic table, and each constituent binary system (Ti-Zr, Zr-Hf, and Hf-Ti) is known to form a complete solid solution across all temperature and composition ranges [39–41]. Furthermore, all three elements exhibit an allotropic transformation from a high-temperature BCC structure to a low-temperature HCP structure. Based on this chemical and crystallographic similarity, the Ti-Zr-Hf ternary system is expected to be an ideal candidate for forming a stable, single-phase HCP solid-solution without the formation of complex intermetallic compounds. *This design rationale is corroborated by prior work on quaternary Ti-Zr-Hf-Nb refractory HEAs, in which substituting Hf with the isoelectronic Group 4 elements Ti and Zr was shown by CALPHAD-guided design to markedly enhance single-phase stability at intermediate temperatures [42]; the present work extends this principle to its logical limit by removing the BCC-stabilizing element entirely.*

To theoretically validate this concept, the Ti-Zr-Hf ternary phase diagram was calculated using the CALPHAD simulation, implemented via Thermo-Calc software with the TCHEA3 database [43]. The results are presented in Fig. 1. Fig. 1**(a)** shows a three-dimensional representation of the phase diagram, constructed from a series of vertical sections calculated by varying the Ti concentration from 0 to 100 at.%. The diagram reveals that both the high-temperature BCC phase (β, green region) and the low-temperature HCP phase (α, blue region) form single-phase solid solution fields across the entire ternary composition range. This calculation confirms that the Ti-Zr-Hf system can serve as an excellent foundational system for forming concentrated HCP solid solutions. For visual clarity, the vertical sections in Fig. 1**(a)** are shown in 20 at.% increments of Ti; more detailed diagrams in 10 at.% increments are provided in Supplementary **Figure S1**.

Fig. 1**(b)** displays a vertical section of the phase diagram for the $Ti_{33.3}Zr_{66.7-x}Hf_x$ compositions, which constitute the representative composition series examined in this study. This diagram illustrates the variation in phase transformation temperatures as the ratio of Zr to Hf is altered at a fixed Ti content of 33.3 at.%. According to the calculations, the equiatomic ($Ti_{33.3}Zr_{33.3}Hf_{33.3}$) alloy is predicted to begin solidifying from the liquid phase into a BCC solid phase at approximately 2038 K and subsequently transform into the HCP phase at ≈1250 K. Notably, the calculation reveals a very narrow solidification range. This suggests that segregation of the constituent elements during solidification is likely to be suppressed, promoting the formation of a chemically homogeneous microstructure. This aspect will be discussed further in conjunction with the experimental results in the following section.

3.2. Microstructure and phase transformation behavior of the equiatomic $Ti_{33.3}Zr_{33.3}Hf_{33.3}$ alloy

To experimentally validate the phase stability predicted by the thermodynamic calculations, an equiatomic $Ti_{33.3}Zr_{33.3}Hf_{33.3}$ alloy was fabricated and characterized. Fig. 2 presents a comprehensive

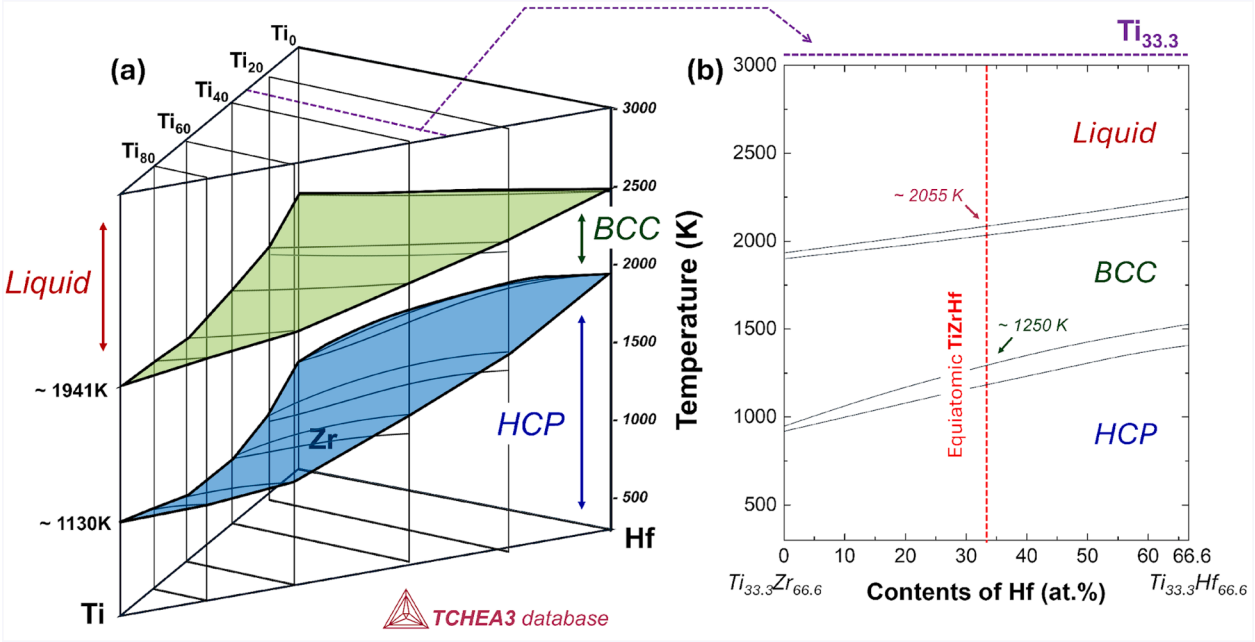


Fig. 1. Calculated phase stability of the Ti-Zr-Hf ternary alloy system. (a) Three-dimensional ternary phase diagram of Ti-Zr-Hf calculated using thermo-calc software (TCHEA3 database). The phase transformation surfaces for the high-temperature BCC phase and the low-temperature HCP phase are highlighted in green and blue, respectively. (b) A vertical section for the $Ti_{33.3}Zr_{66.7-x}Hf_x$ system, showing the phase fields for a constant Ti content of 33.3 at.%. The red dashed line indicates the equiatomic TiZrHf composition. More detailed vertical sections for other Ti compositions are provided in **Supplementary Figure S1**.

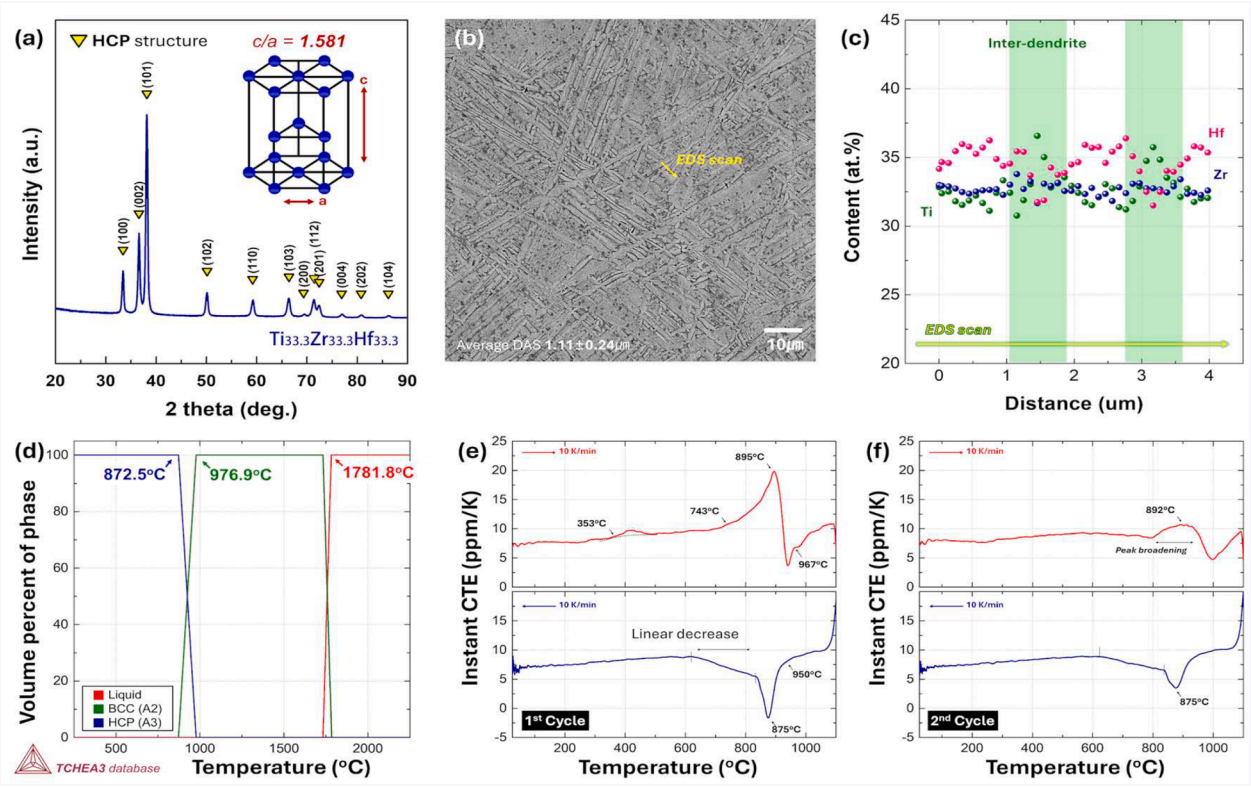


Fig. 2. Microstructure, phase stability, and thermomechanical behavior of the as-cast equiatomic $Ti_{33.3}Zr_{33.3}Hf_{33.3}$ HEA. (a) XRD pattern confirming the single-phase HCP structure of the as-cast alloy. The inset shows the HCP unit cell and the measured c/a ratio of 1.581. (b) BSE image revealing the dendritic microstructure. The contrast variation indicates chemical segregation resulting from solidification. The yellow line indicates the path of the EDS line scan shown in (c). (c) EDS line scan across the dendrite and inter-dendrite regions, quantifying the segregation of Hf to the dendrite cores and Ti to the interdendritic regions. (d) Equilibrium phase fraction diagram as a function of temperature for the equiatomic composition, calculated using Thermo-Calc software (TCHEA3 database). (e, f) Instantaneous CTE measured by dilatometry during the (e) first and (f) second thermal cycles at a heating/cooling rate of 10 K/min, showing the phase transformation behavior. The difference between the cycles indicates the homogenization of the as-cast structure during the first heating.

microstructural and phase analysis of this alloy in the as-cast condition. The X-ray diffraction (XRD) pattern in Fig. 2**(a)** confirms the crystal structure of the as-cast alloy. All major diffraction peaks are indexed to a single-phase HCP crystal structure, with no evidence of secondary phases such as intermetallic compounds or a residual BCC phase. This result is in excellent agreement with the thermodynamic calculations, which predicted the formation of a stable HCP solid solution at room temperature. The c/a ratio, calculated from the lattice parameters determined by the XRD pattern (e.g., (101) peak at 38.147°), is approximately 1.581. This value is lower than the ideal c/a ratio for an HCP structure (1.633) and is also slightly smaller than that of the commercial Ti-6Al-4V alloy (≈1.59) [44].

Fig. 2**(b)** shows a backscattered electron (BSE) image of the as-cast alloy, revealing a typical equiaxed dendritic solidification structure. The fine microstructure is characterized by a primary dendrite arm spacing (DAS) of approximately 1.11 ± 0.24 μm. To evaluate the chemical homogeneity, an energy-dispersive X-ray spectroscopy (EDS) line scan was performed along the yellow arrow in Fig. 2**(b)**, with the corresponding compositional profiles shown in Fig. 2**(c)**. While the overall composition maintains the equiatomic ratio, dendrite-interdendrite segregation is still confirmed. Hf, having the highest melting point among the constituents (2233°C), is enriched in the dendrite cores, which solidify first. Conversely, Ti, with the lowest melting point (1668°C), is predominantly found in the last-to-solidify interdendritic regions. Zr exhibits a relatively uniform distribution. Nevertheless, the maximum compositional deviation for each element remains within ±5 at.% of the average, indicating that severe segregation was suppressed. This is consistent with the narrow solidification range predicted by the CALPHAD simulations.

The observed phase and microstructure are further supported by the equilibrium phase fraction diagram for the equiatomic composition, shown in Fig. 2**(d)**. This diagram illustrates the phase evolution upon cooling: Liquid → BCC(β) → HCP(α), without the formation of any other phases. The solid-state phase-transformation (α ↔ β) was investigated experimentally via dilatometry. Fig.s 2**(e)** and **(f)** display the instantaneous coefficient of thermal expansion (CTE) during the first and second thermal cycles, respectively. In the first heating cycle (Fig. 2**(e)**), a distinct endothermic peak corresponding to the HCP(α)→BCC(β) transformation is observed at approximately 895°C. This primary transformation temperature is reproducible in the second cycle (Fig. 2**(f)**). Interestingly, the first cycle also reveals a minor peak at a lower temperature (around 353°C). This peak is likely attributable to either a localized phase transformation within the Ti-rich interdendritic regions or the relief of as-cast internal stresses. This feature is absent in the second cycle, suggesting that the microstructure becomes more homogeneous after the initial thermal treatment. The disappearance of the low-temperature peak and the slight broadening of the main transformation peak in the second cycle support the conclusion that the initial non-equilibrium state is effectively homogenized.

3.3. Crystal structure variation with composition

Following the confirmation of a single-phase HCP structure in the equiatomic alloy, the investigation was expanded to a wider compositional range to systematically map the phase stability and microstructural evolution. For this purpose, a series of alloys with varying elemental proportions were fabricated and characterized in the as-cast state. Fig. 3 comprehensively presents the crystal structure analysis for

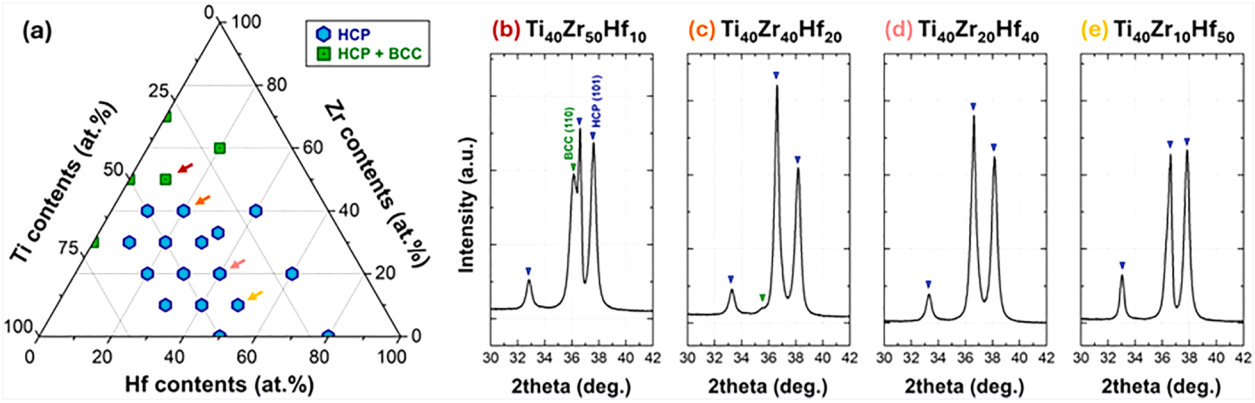


Fig. 3. Crystal structure of the as-cast Ti-Zr-Hf alloys as a function of composition. (a) Ternary diagram illustrating the experimentally determined crystal structures. Alloys exhibiting a single-phase HCP structure are marked with blue hexagons, while dual-phase (HCP + BCC) alloys are indicated by green squares. The colored arrows point to the specific compositions ($Ti_{40}Zr_{50}Hf_{10}$, $Ti_{40}Zr_{40}Hf_{20}$, $Ti_{40}Zr_{20}Hf_{40}$, and $Ti_{40}Zr_{10}Hf_{50}$) analyzed in (b-e). **(b-e)** Representative X-ray diffraction (XRD) patterns for selected alloys with a constant Ti content of 40 at.%. The patterns show a transition from a dual-phase HCP + BCC structure in **(b)** to a single-phase HCP structure in **(d)** and **(e)**. Peaks corresponding to the HCP and BCC phases are indexed with blue and green triangles, respectively.

the fabricated alloys. The ternary diagram in Fig. 3**(a)** maps the experimentally determined phases, confirming that a stable single-phase HCP solid solution (blue hexagons) forms over a vast majority of the investigated compositions. This result provides strong evidence that the Ti-Zr-Hf system is an excellent platform for designing HCP HEAs. A deviation from this single-phase stability was observed in the

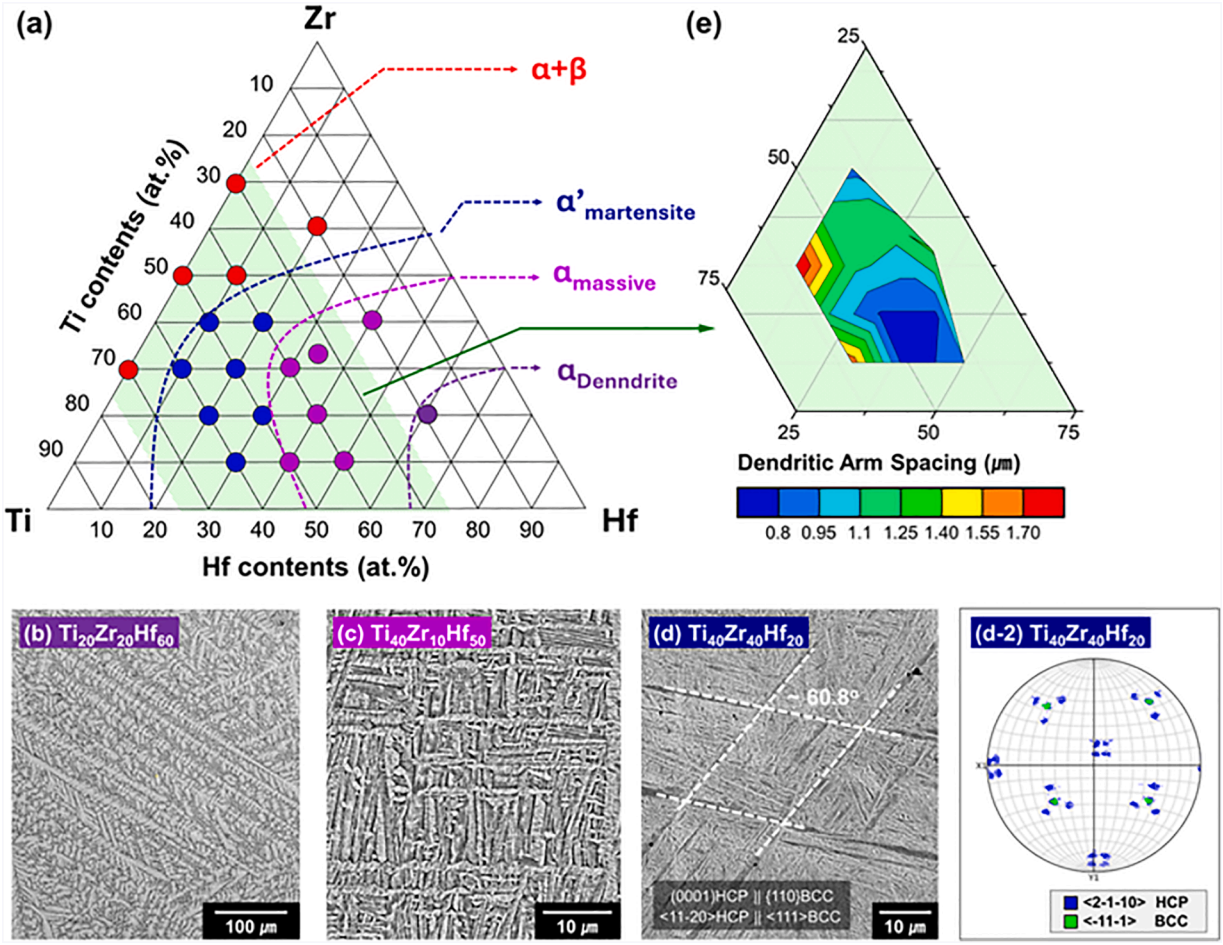


Fig. 4. Composition-dependent microstructural evolution in the as-cast Ti-Zr-Hf HEAs. (a) Ternary diagram mapping the observed as-cast microstructural morphologies. The microstructures are classified into dendritic ($\alpha_{Dendrite}$), massive ($\alpha_{massive}$), martensitic (α'), and dual-phase (α+β). **(b-d)** Representative SEM micrographs of the distinct morphologies: **(b)** a dendritic structure in the Hf-rich $Ti_{20}Zr_{20}Hf_{60}$ alloy; **(c)** a Widmanstätten structure in the $Ti_{40}Zr_{10}Hf_{50}$ alloy; and **(d)** a lath martensitic structure in the $Ti_{40}Zr_{40}Hf_{20}$ alloy. **(d-2)** The pole figure from EBSD analysis of the $Ti_{40}Zr_{40}Hf_{20}$ alloy confirms the Burgers orientation relationship ((0001)α || {110}β; <11-20>α || <111>β) between the parent BCC (β) and product HCP (α) phases. **(e)** A contour map showing the variation of the characteristic microstructural feature size (dendrite arm or lath spacing) as a function of alloy composition.

compositional region characterized by low Hf and high Ti/Zr contents (green squares), where a dual-phase (HCP+BCC) structure was identified. The retention of some high-temperature β phase is consistent with the preceding thermodynamic analysis, which predicted that Ti and Zr act as relative BCC stabilizers compared to Hf.

In addition to the phase constitution, the lattice parameters of the HCP phase were determined for every composition examined; the resulting c/a ratios are compiled in ***Table S2*** *and mapped over the ternary composition space in Supplementary* ***Figure S2****. Notably, the c/a ratio does not vary monotonically with any single elemental content: at a fixed Hf content, for example, it varies by up to 0.035 depending on the Ti/Zr balance, a range comparable to the total variation observed across the entire dataset. The c/a ratio therefore constitutes a crystallographic degree of freedom that is not simply a proxy for composition, a point examined further in* Section 4.

To examine this phase transition in greater detail, the XRD patterns of alloys with a constant Ti content of 40 at.% are presented in Fig. 3**(b-e)**. The $Ti_{40}Zr_{50}Hf_{10}$ alloy (Fig. 3**(b)**), in contrast to the single-phase equiatomic alloy, exhibits a distinct BCC (110) peak alongside the (002) HCP peaks. However, upon increasing the Hf content at the expense of Zr, the intensity of this BCC peak sharply decreases in the $Ti_{40}Zr_{40}Hf_{20}$ alloy (Fig. 3**(c)**). Here, quantitative analysis via Rietveld refinement for $Ti_{40}Zr_{40}Hf_{20}$ indicated a BCC phase fraction of less than 1%, a negligible level. In the $Ti_{40}Zr_{20}Hf_{40}$ (Fig. 3**(d)**) and $Ti_{40}Zr_{10}Hf_{50}$ (Fig. 3**(e)**) alloys, the BCC-related peaks disappear entirely, confirming the formation of a complete single-phase HCP structure. This series of results clearly demonstrates that as the content of Hf, a potent HCP stabilizer, decreases, the retention of the high-temperature BCC phase is more pronounced.

Although the XRD analysis confirmed a single-phase HCP crystal structure for most alloys, their microstructural morphologies, as observed via SEM, were remarkably diverse and highly dependent on composition. Fig. 4**(a)** provides a microstructural map summarizing these observations. Overall, the as-cast alloys exhibited a systematic transition in their dominant microstructural features, transitioning from solidification-induced dendritic morphologies ($\alpha_{Dendrite}$) to solid-state transformation products such as massive ($\alpha_{massive}$) and martensitic (α′) structures as the composition moved from the high-Hf region towards the high Ti region. Specifically, in the high-Hf $Ti_{20}Zr_{20}Hf_{60}$ alloy, a typical dendritic structure was observed, as shown in Fig. 4**(b)**. The relatively rounded morphology of the dendrite interfaces suggests that the structure formed via diffusional growth, driven by compositional partitioning during solidification. This alloy displayed a coarse primary dendrite arm spacing (DAS) averaging 11.3 μm. In contrast, as the Hf content decreased, the microstructure progressively transformed into an acicular, or needle-like, morphology. Fig. 4**(c)** shows the microstructure of the $Ti_{40}Zr_{10}Hf_{50}$ alloy, which is representative of a Widmanstätten or basket-weave structure. This morphology, consisting of intersecting laths of the α phase, is commonly associated with massive transformations involving short-range diffusion. In the $Ti_{40}Zr_{40}Hf_{20}$ alloy, with even lower Hf content, the transformation mechanism changes to a diffusionless process, resulting in a highly ordered, coarse lath martensitic structure (Fig. 4**(d)**). These laths are observed to intersect at an angle of approximately 60°, consistent with the self-accommodating nature of martensitic transformations in HCP structures, which minimizes strain energy [45]. This crystallographic relationship was definitively confirmed by the EBSD pole figure analysis shown in Fig. 4**(d-2)**.

While the Widmanstätten and martensitic structures may appear morphologically similar in Fig. 4 — both consisting of fine, intersecting lath features — STEM-EDS analyses reveal that they are fundamentally distinct in nature. Fig. 5 presents the STEM images and EDS maps of (a) $Ti_{40}Zr_{10}Hf_{50}$ and (b) $Ti_{40}Zr_{40}Hf_{20}$ alloys. In the Widmanstätten structure (Fig. 5**(a)**), a clear Ti-rich substructure is observed along the lath

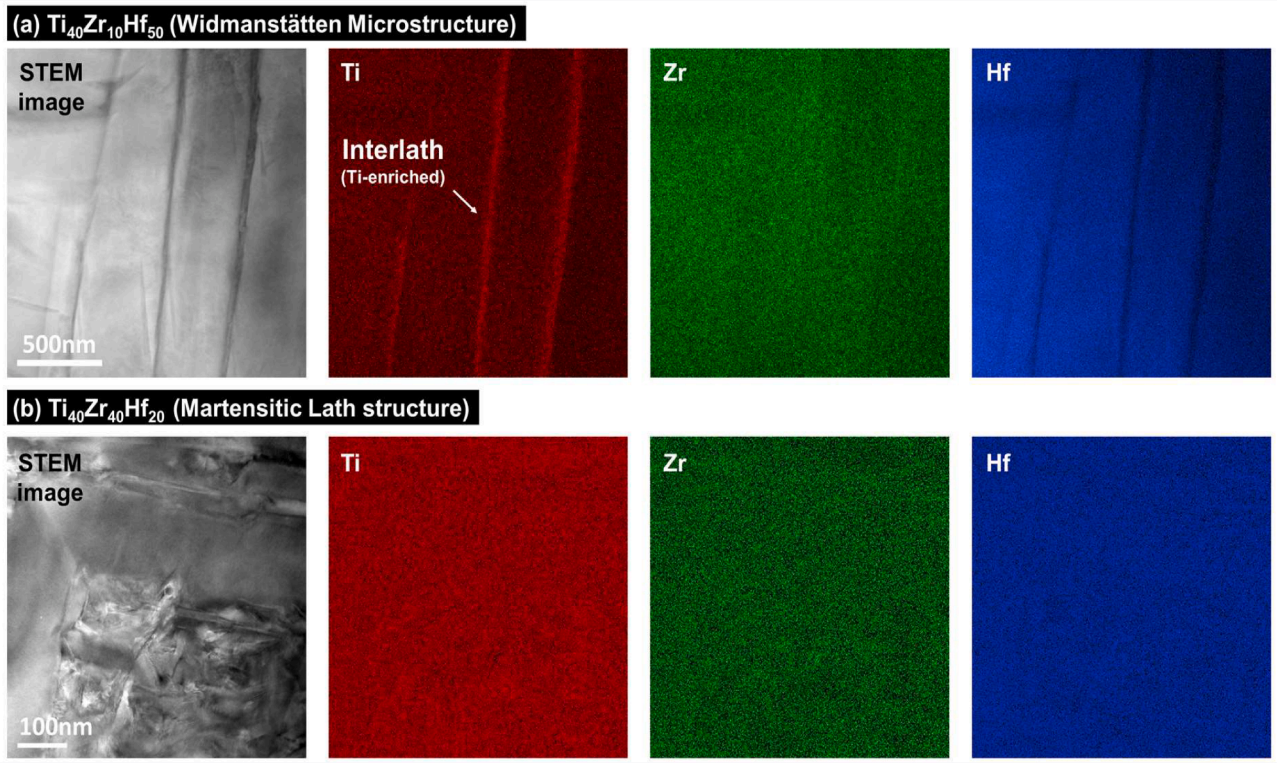


Fig. 5. STEM-EDS analyses revealing the distinct elemental distributions underlying the Widmanstätten and martensitic structures. (a) STEM image and corresponding Ti, Zr, and Hf elemental maps of the Widmanstätten structure in the $Ti_{40}Zr_{10}Hf_{50}$ alloy. A Ti-enriched interlath substructure is clearly resolved, accompanied by relative Hf depletion in the interlath regions, while Zr remains relatively uniformly distributed. **(b)** STEM image and corresponding elemental maps of the martensitic lath structure in the $Ti_{40}Zr_{40}Hf_{20}$ alloy, showing no measurable Ti/Zr/Hf partitioning across adjacent laths within the spatial resolution of STEM-EDS, consistent with a diffusionless transformation process.

boundaries. The lower-melting-point Ti is preferentially segregated into these interlath regions, while Hf is correspondingly enriched within the lath interiors; Zr, in contrast, remains relatively uniformly distributed across both regions. This pronounced Ti/Hf partitioning indicates substantial elemental redistribution during transformation, thereby supporting a diffusion-assisted transformation pathway. In contrast, the martensitic lath structure (Fig. 5**(b)**) exhibits no measurable Ti/Zr/Hf partitioning across adjacent laths within the spatial resolution of STEM-EDS, consistent with a diffusionless transformation process in which the parent and product phases share an identical composition. These compositional observations provide direct evidence for the distinct transformation mechanisms that were initially inferred from morphology and transformation temperature alone, confirming that the superficially similar lath morphologies in fact arise from entirely different — diffusional versus diffusionless — transformation origins. The analysis revealed that the classical solidification and subsequent solid-state transformation pathways in the Ti-Zr-Hf system are highly tunable through compositional control. Detailed microstructures for all other alloy compositions are provided in Supplementary **Figure S3**.

3.4. Mechanical Properties Evaluation of Ti-Zr-Hf Alloys

To establish a clear link between alloy composition and mechanical properties, the hardness and elastic modulus of each alloy were systematically evaluated using nanoindentation. To ensure statistical robustness, the results presented in the ternary contour maps of Fig. 6 represent the average of at least 225 measurements per composition. (The detailed indentation curves are illustrated in supplementary **Figure S4**.) Fig. 6**(a)** exhibits that the hardness is highly sensitive to the alloy's composition, exhibiting a clear and systematic trend. The lowest hardness, approximately 4.3 GPa, is observed in the Ti-rich region. As the Ti content decreases and the Hf increases, the hardness progressively increases, reaching a maximum value 5.5 GPa in the high Hf-region. This trend is likely attributable to enhanced solid-solution strengthening, as the larger atomic radii of Zr and Hf relative to Ti induce more severe lattice distortion. The reduced elastic modulus, shown in Fig. 6**(b)**, demonstrates a nearly identical compositional dependence. It increases from a minimum of about 88 GPa in the Ti-rich corner to a maximum of 118 GPa as the Zr and Hf contents increase, indicating that these elements contribute to enhancing both the strength and stiffness of the alloy.

The equiatomic $Ti_{33.3}Zr_{33.3}Hf_{33.3}$ alloy was selected as the most representative composition for mechanical characterization, as it occupies the geometric center of the ternary composition space and serves as the standard benchmark in HEA research. Furthermore, to assess the bulk mechanical properties and underlying deformation mechanisms, uniaxial meso-scale tensile tests were performed at room temperature on the representative equiatomic alloy. The resulting engineering stress-strain curves, shown in Fig. 7**(a)**, demonstrate the alloy's outstanding mechanical properties. The tests, repeated three times to confirm reproducibility, show a very high yield strength (YS) of approximately 1140 MPa and an ultimate tensile strength (UTS) that reaches 1250 MPa. Crucially, the alloy also exhibits excellent elongation to fracture of larger than 16%, confirming that a superior combination of high strength and significant ductility was achieved.

To understand the origin of this excellent combination of strength and ductility, the microstructure of the fractured specimen after the tensile test was analyzed in detail, as shown in Fig. 7**(b)**. The main plastic deformation mechanism was confirmed to be the activation of deformation-induced twinning. It is clearly observed that numerous fine twins were formed in a parallel lamellar fashion inside the coarse dendritic structure aligned in the loading direction. This analysis is clearly supported by the inserted EBSD misorientation profile. The misorientation measured across the twin boundary is approximately 86°, which exactly matches the unique crystallographic feature of {10-12} extension twins that typically appear in HCP metals [46].

Meanwhile, to track the influence of the crystallographic difference of the HCP structure on the deformation behavior, two additional fully-HCP compositions with the highest and lowest c/a ratios were tensile tested: the $Ti_{50}Zr_{20}Hf_{30}$ alloy (c/a = 1.615) and the $Ti_{50}Zr_{40}Hf_{10}$ alloy (c/a = 1.578); the detailed c/a ratios of all other alloys are provided in Supplementary **Table S2**. As shown in Fig. 8**(a)**, the two alloys exhibited comparable yield strengths but distinct work-hardening responses, with the high-c/a alloy sustaining a markedly higher work-hardening rate over an extended strain range (Fig. 8**(b)**).

To identify the deformation features responsible for this difference,

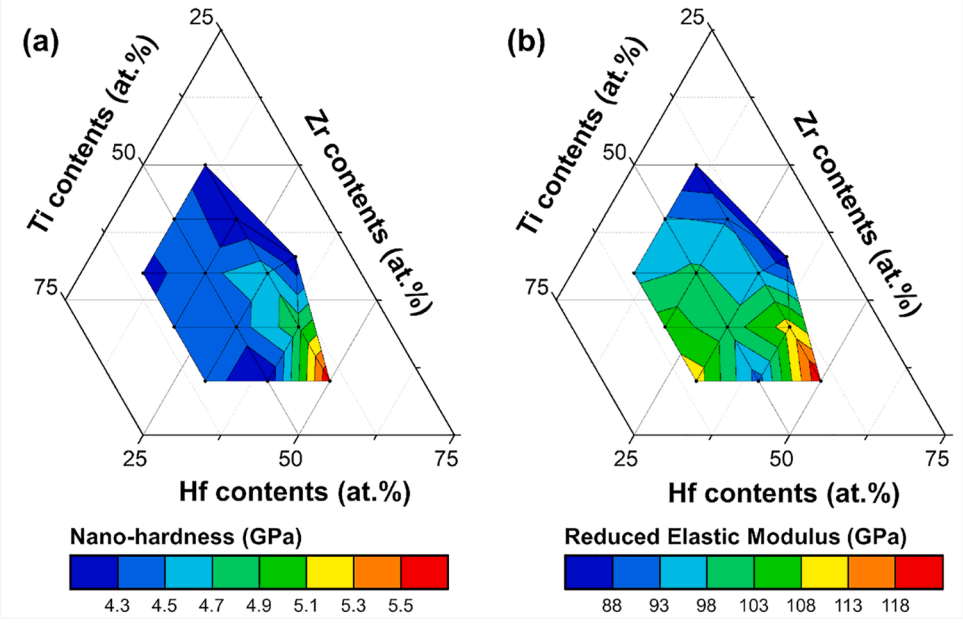


Fig. 6. Compositional dependence of mechanical properties of the as-cast Ti-Zr-Hf HEAs measured by nanoindentation. Ternary contour maps showing the **(a)** nano-hardness and **(b)** reduced elastic modulus as a function of alloy composition. Both properties exhibit a clear trend, decreasing from the Hf-rich corner towards the Ti-Zr binary edge. (The hardness and elastic modulus values with their corresponding standard deviations for all compositions are provided in Supplementary **Table S1**.)

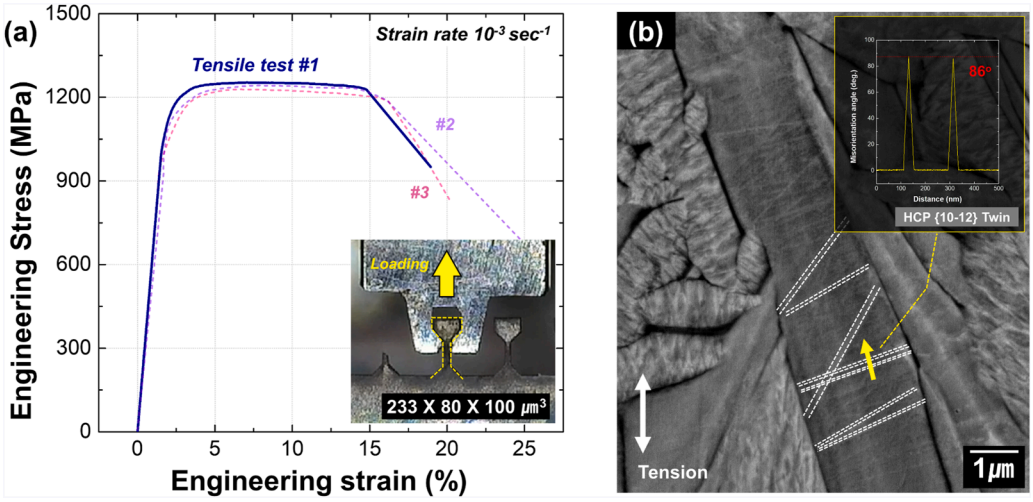


Fig. 7. Mechanical properties and deformation mechanism of the as-cast equiatomic TiZrHf HEA. (a) Representative engineering stress-strain curves from uniaxial meso-scale tensile tests conducted at a strain rate of 10^{-3} s^{-1}. The alloy exhibits a high yield strength of 1140 MPa and excellent elongation to fracture exceeding 16%. The inset shows an SEM image of the meso-scale tensile specimen used for the test. **(b)** SEM micrograph of the specimen after fracture, revealing parallel lamellar features at a specific angle to the tensile axis (white arrow). The inset EBSD misorientation profile, measured across these features, shows a characteristic misorientation angle of ≈86°. This is a definitive signature of {10-12} extension twins in HCP structures, indicating that deformation-induced twinning is the primary plastic deformation mechanism.

the microstructures of the fractured specimens were examined using the electron channeling contrast imaging (ECCI) technique under back-scattered electron (BSE) mode. The low-c/a $Ti_{50}Zr_{40}Hf_{10}$ alloy, which has a c/a ratio nearly identical to that of the equiatomic alloy, deformed via a similar twinning-dominated mechanism, with deformation twins clearly observed within the lath structure. In addition, a closer inspection of the boxed region of Fig. 8**(c)** revealed that numerous stacking faults were also present in the surrounding matrix, as shown in detail in Fig. 8**(d)** [47].

In contrast, the high-c/a $Ti_{50}Zr_{20}Hf_{30}$ alloy exhibited a distinctly different deformation response. As shown in **Figure 8(e)**, no clear evidence of deformation twinning was observed; instead, the plastic deformation was accommodated predominantly by slip. A magnified view of the boxed region (Fig. 8**(f)**) reveals well-defined slip bands developed within the martensitic lath structure, confirming that the laths were deformed through the activation of these slip bands [48]. The slip appears to be largely confined within individual laths, with the lath boundaries acting as barriers that restrict the propagation of slip across the structure. This confinement of slip is expected to promote the accumulation of dislocations within the laths, which is consistent with the elevated work-hardening rate observed for this composition (Fig. 8 **(b)**).

4. Discussion

The Ti-Zr-Hf alloys investigated in this study, despite predominantly consisting of a single-phase HCP crystal structure, exhibited a remarkably diverse array of as-cast microstructures, systematically transitioning from dendritic to Widmanstätten and martensitic morphologies as a function of composition (Fig. 4). This systematic microstructural evolution can be mechanistically understood as a direct consequence of the kinetic competition between diffusional (e.g., dendritic, massive) and diffusionless (martensitic) solid-state transformations. Since all alloys were fabricated under identical casting conditions, they were subjected to nominally identical thermal history, effectively fixing the cooling trajectory on a time-temperature plot. Of course, minor variation may exist with experimental uncertainties. Under this constant kinetic constraint, the final microstructure is dictated solely by the intrinsic transformation behavior of the material. Therefore, the observed morphological diversity—from dendritic to martensitic—is not an artifact of processing but rather a direct manifestation of how compositional variations, particularly the Hf content, systematically alter the thermodynamic driving forces and atomic mobilities that govern the CCT characteristics of each alloy.

The thermodynamic origin of this compositional influence can be quantitatively understood by examining the relative phase stabilities of the constituent elements, as derived from the phase diagram in Fig. 1. A useful metric for evaluating the stability of the high-temperature BCC phase is the normalized temperature window over which it exists, defined as the ratio of the BCC stability range ($\Delta T_\beta = T_m - T_{\beta\to\alpha}$) to the melting point ($T_m$). For pure Hf, with $T_m \approx 2506$ K and $T_{\beta\to\alpha} \approx 1950$ K, the stability ratio ($\Delta T_\beta / T_m$) is approximately 0.22. In contrast, pure Ti ($T_m \approx 1941$ K, $T_{\beta\to\alpha} \approx 1130$ K) exhibits a stability ratio of approximately 0.42. This quantitative comparison reveals that the BCC phase field in Ti is thermodynamically stable over a significantly larger fraction of its solid-state temperature range compared to Hf. Consequently, Hf functions as a potent HCP stabilizer within the Ti-Zr-Hf system; its addition systematically raises the β→α transformation temperature, thereby contracting the BCC phase field and expanding the stability region of the low-temperature HCP phase [49]. This fundamental thermodynamic effect is the primary driver for the observed changes in transformation kinetics.

The mechanistic link between the Hf content and the resulting microstructure is interpreted using the schematic Continuous Cooling Transformation (CCT) diagrams proposed in Fig. 9. These diagrams are presented as a conceptual framework that captures the observed microstructural trends, rather than as experimentally measured CCT curves. Such an approach is particularly valuable in the early-stage exploration of complex alloy systems, as it establishes the mechanistic link between composition and transformation behavior that can guide subsequent quantitative investigation. These diagrams illustrate how a fixed cooling trajectory—representative of the rapid water-quenching employed in this study—intersects with CCT curves that are themselves a strong function of composition. Let us first consider the low-Hf case, depicted in Fig. 9**(a)**. In these alloys, the significant thermodynamic stability of the parent β-BCC phase kinetically retards the onset of diffusional α-HCP transformations. This sluggishness effectively shifts the C-shaped noses for both dendritic growth and massive transformation (occurring at intermediate temperatures) to longer times [50]. Consequently, the rapid, fixed cooling path is proposed bypasses

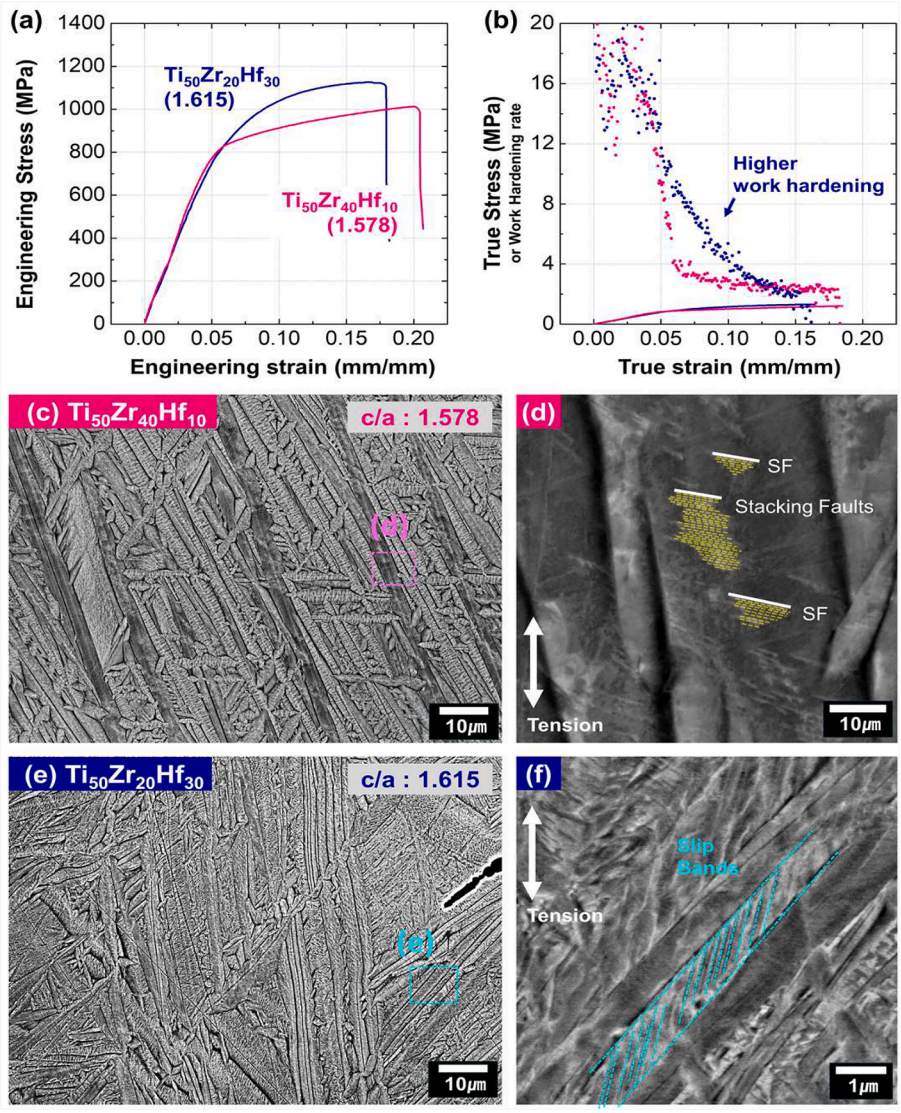


Fig. 8. Effect of the c/a ratio on the mechanical properties and deformation mechanisms of as-cast Ti-Zr-Hf HEAs. (a) Representative engineering stress-strain curves from uniaxial meso-scale tensile tests of the two alloys. The two alloys exhibit comparable yield strengths, with the high-c/a alloy showing a higher ultimate strength. (b) Corresponding work-hardening rate curves, showing the markedly higher work-hardening rate of the high-c/a alloy. (c) SEM micrograph of the fractured $Ti_{50}Zr_{40}Hf_{10}$ (c/a = 1.578) specimen, deformed via a twinning-dominated mechanism, and (d) a magnified view of the boxed region, revealing numerous stacking faults (SF) in the surrounding matrix. (e) SEM micrograph of the fractured $Ti_{50}Zr_{20}Hf_{30}$ (c/a = 1.615) specimen, showing no clear evidence of deformation twinning, and (f) a magnified view of the boxed region, revealing well-developed slip bands confined within the martensitic lath structure. These results demonstrate that the active deformation mode varies with the c/a ratio and the underlying microstructure, ranging from twinning- and stacking-fault-mediated plasticity to confined slip, with the latter promoting dislocation accumulation and an elevated work-hardening rate.

these diffusional transformation regimes. The alloy, therefore, remains in a metastable, supercooled β phase until the temperature drops below the Martensite start (M_s) temperature. Below M_s, long-range atomic diffusion is kinetically frozen, and the only viable pathway for the system to lower its free energy is through a diffusionless, cooperative shear transformation. This martensitic transformation is expected to be crystallographically constrained, proceeding via a specific lattice shear that maintains the Burgers orientation relationship between the parent β and product α' phases to minimize interfacial strain energy. This sequence of events—the kinetic suppression of diffusional pathways followed by a diffusionless shear transformation at low temperatures— provides a plausible explanation for the formation of the observed martensitic microstructures in the low-Hf alloys.

Conversely, as the Hf content increases, this kinetic balance is systematically shifted. The addition of Hf, a more potent HCP stabilizer than Ti or Zr, raises the equilibrium β→α transformation temperature. This elevation has a twofold effect: first, it increases the thermodynamic driving force ($\Delta G_{\beta\rightarrow\alpha}$) for diffusional transformation at any given temperature, thereby shifting the C-curves for both massive and dendritic growth to shorter times (to the left, as depicted in Fig. 9**(b)**). Second, the significant lattice distortion introduced by the large Hf atoms can be argued to increase the energetic barrier for the cooperative shear required for martensitic transformation, effectively suppressing the M_s temperature. The net result is that the kinetic window for diffusion-mediated transformation widens at the expense of the martensitic one. The fixed cooling path, which previously bypassed all diffusional regimes, now intersects the C-curve for massive transformation, leading to the formation of the Widmanstätten and basket-weave microstructures observed in the mid-Hf alloys.

In the high-Hf regime, shown in Fig. 9**(c)**, the β→α transformation temperature is raised to a point where it occurs at very high homologous temperatures, approaching the solidus. At these elevated temperatures,

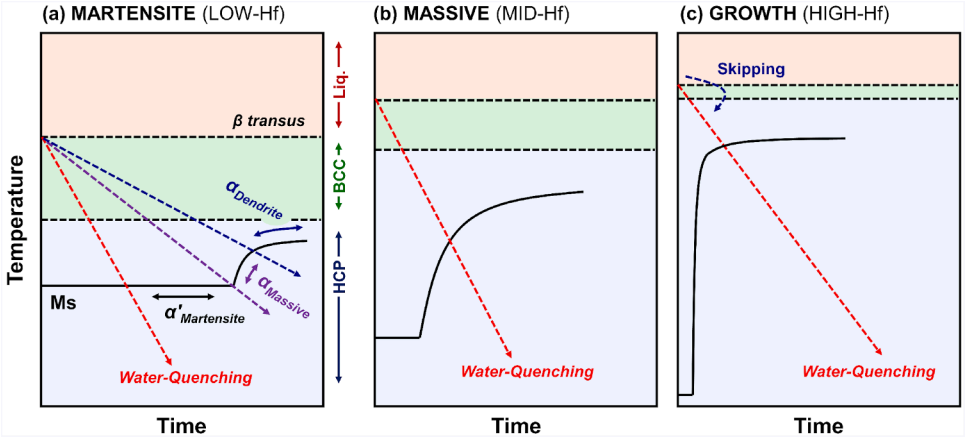


Fig. 9. Schematic Continuous Cooling Transformation (CCT) diagrams illustrating the proposed mechanism for microstructure formation in Ti-Zr-Hf alloys as a function of Hf content. (a) In low-Hf alloys, the CCT curves for diffusional transformations (dendritic and massive) are located at longer times. A rapid cooling rate, such as water-quenching, bypasses these transformations, allowing the alloy to cool below the Martensite start (M_s) temperature and form a martensitic (α') structure. (b) In mid-Hf alloys, the CCT curve for the massive transformation shifts to shorter times. The cooling path now intersects this curve, leading to the formation of a massive (α_massive) microstructure. (c) In high-Hf alloys, the transformation kinetics for diffusional growth become extremely rapid. The CCT curve is shifted far to the left, and even water-quenching cannot suppress the high-temperature diffusional transformation, resulting in a dendritic or Widmanstätten growth structure.

atomic mobility becomes exceptionally high, as dictated by the Arrhenius relationship. Consequently, kinetic limitations on long-range diffusion are virtually eliminated. The system is no longer constrained to non-equilibrium pathways such as massive or martensitic transformations; instead, it can readily achieve a lower energy state through full compositional partitioning via diffusion. This dominance of diffusional processes is consistent with the formation of the coarse, equilibrium dendritic microstructures observed in alloys such as $Ti_{20}Zr_{20}Hf_{60}$.

The mechanical properties of this alloy system are intrinsically linked to the composition and the resultant microstructural features. A compelling inverse relationship emerges when comparing the characteristic microstructural length scale (Fig. 4) and the hardness (Fig. 6). The fine lath boundaries prevalent in the martensitic and massive structures (lath width≈0.8-1.3 μm) evidently act as potent obstacles to dislocation motion, analogous to a Hall-Petch strengthening mechanism, resulting in high hardness values ≈5.5 GPa [51]. In contrast, the much coarser dendritic structures (DAS≈11.3 μm) offer fewer barriers, leading to a correspondingly lower hardness of approximately 4.2 GPa. This trend is underpinned by atomic-scale solid-solution strengthening, a primary strengthening mechanism in HEAs. The significant disparity in atomic radii between Ti (147 pm), Zr (160 pm), and Hf (159 pm) generates a severe, localized strain field within the crystal lattice, which strongly impedes dislocation glide [52] The strong positive correlation between hardness and elastic modulus observed in Fig. 6 further suggests that the addition of Zr and Hf enhances the average interatomic bonding strength of the alloy, contributing to both modulus and strength. The magnitude of this solid-solution strengthening can be quantitatively validated; applying Tabor's rule ($H \approx 3 \times \sigma_y$) to the H data yields estimated YS in the GPa range, which is in excellent agreement with the high YS (≈1.2 GPa) directly measured from the meso-scale tensile tests of the equiatomic alloy (Fig. 7) [53,54].

Beyond the equiatomic composition, the broad single-phase HCP field of the Ti-Zr-Hf system permits the c/a ratio to be varied appreciably across compositions, raising the question of how this crystallographic parameter influences the operative deformation mechanisms. *A comparison between two alloys selected to maximize the c/a contrast at a fixed Ti content of 50 at.% (Fig. 8) reveals a clear divergence in their deformation responses. The low-c/a $Ti_{50}Zr_{40}Hf_{10}$ alloy (1.578) deformed through a combination of deformation twinning and stacking fault formation.* In contrast, the high-c/a $Ti_{50}Zr_{20}Hf_{30}$ alloy (1.615) showed no appreciable twinning and instead accommodated plasticity through slip bands confined within its martensitic laths, yet exhibited a markedly higher work-hardening rate.

*Because Ti, Zr, and Hf are homologous Group 4 elements whose binaries form complete solid solutions without intermetallic compounds [39–41], the two alloys are not distinct materials but two points within one continuous HCP solid solution (Figures 1(a) and 3(a)), differing only in the lattice parameters of that solution. The substitution here is exclusively Zr ↔ Hf, two elements of nearly identical atomic radius and identical valence electron concentration, so the atomic size mismatch changes by only 0.13%p (δ = 4.18% versus 4.05 %); the comparable yield strengths of the two alloys confirm that solid-solution strengthening is essentially unchanged. Nor is the c/a ratio a proxy for the Hf content that governs the transformation pathway: at fixed Hf content it varies by up to 0.035 with the Ti/Zr balance (**Supplementary Figure S2**), a range comparable to the difference between the two alloys examined here. The observed transition follows quantitatively from this parameter. The characteristic shear (**s**) of the {10-12}⟨-1011⟩ twinning mode can be calculated like below [4,55]:*

$$s = \frac{|3-(c/a)^2|}{\sqrt{3}(c/a)}$$

*This shear value falls from 0.187 to 0.140 between the two alloys, so that each twin accommodates proportionally less shear strain at the higher c/a. Independently, an increasing c/a ratio lowers the critical resolved shear stress for basal slip relative to prismatic slip, the trend that distinguishes basal-dominated metals above the ideal ratio (Zn, Cd) from the prismatic-dominated Group 4 metals below it [55,56], thereby expanding the easy-slip capacity and reducing the driving force for twin nucleation. Both effects act in the same direction, and the abundant stacking faults observed alongside twins in the low-c/a alloy (**Figure 8(d)**) are consistent with the lower SFE expected at lower c/a [57].*

The two alloys also differ in as-cast morphology (Fig. 4), but this difference is of a different kind than in ferrous systems, where martensite is a genuinely distinct phase stabilized by interstitial supersaturation [51]. In a substitutional Ti-Zr-Hf solid solution, the $\beta \rightarrow \alpha'$ transformation is a diffusionless shear that yields the same HCP structure as the equilibrium α phase [45,49], with the same slip and twinning systems and comparable ductility; martensite here is therefore better regarded as a metastable morphology arising from the kinetic suppression of diffusional transformation than as a structurally distinct phase. What the morphology does control is the internal length scale: the densely distributed lath boundaries of the high-c/a alloy shorten the dislocation mean free path and promote rapid dislocation

accumulation, plausibly accounting for part of its elevated work-hardening rate [48,58]. It is not, however, a mechanism by which twinning can be switched off, since twin activation is governed by the twinning shear, the stacking fault energy, and the availability of competing slip systems — all set by the lattice rather than by the morphology in which it is arranged [4,46,55]. Consistently, the equiatomic alloy twins in a dendritic morphology at c/a = 1.581, close to that of $Ti_{50}Zr_{40}Hf_{10}$, so that twinning is observed across both dendritic and massive structures at low c/a and absent in the martensitic structure at high c/a. The morphology thus contributes to the magnitude of the work-hardening response, while the crystallography determines which deformation mode is available to produce it — making the c/a ratio, readily tunable across the wide single-phase HCP field of this system, an accessible descriptor for tailoring the deformation behavior of HCP HEAs.

5. Conclusion

In this study, we establish a foundational understanding for the development of HCP HEAs using the Ti-Zr-Hf ternary system. Through a combined approach of thermodynamic calculations, fabrication of as-cast alloys with various compositions, and subsequent microstructural and mechanical characterization, the interrelationships between composition, microstructure, and properties were successfully elucidated. The primary conclusions are as follows:

1. The Ti-Zr-Hf system was validated as an ideal model system for developing single-phase HCP HEAs, as it forms a stable solid solution over a wide compositional range without forming any intermediate phases or intermetallic compounds. The focus on as-cast microstructures provides a critical baseline for future processing, including additive manufacturing.
2. The as-cast microstructure is systematically controlled by composition, primarily the Hf content, which dictates the dominant solid-state transformation mechanism. High-Hf alloys favor high-temperature, diffusion-dominant transformations, resulting in dendritic structures. Conversely, low-Hf alloys suppress diffusional kinetics, leading to a diffusionless martensitic transformation. This behavior was rationalized by a conceptual model in which Hf content systematically alters the alloy's intrinsic CCT curve.
3. The mechanical properties exhibit a strong dependence on both composition and the resulting microstructure. The highest hardness (≈5.5 GPa) was observed in $Ti_{40}Zr_{10}Hf_{50}$ alloy, which is associated with the fine massive (Widmanstätten) lath structure. This is a combined result of potent solid-solution strengthening and microstructural refinement (Hall-Petch effect). The equiatomic $Ti_{33.3}Zr_{33.3}Hf_{33.3}$ alloy, in particular, demonstrated an exceptional synergy of high strength (1140MPa) and excellent ductility (>16%), which is attributed to the activation of deformation-induced twinning (TWIP effect). Furthermore, *a comparison of alloys with differing c/a ratios revealed that the operative deformation mode is governed by the crystallography of the HCP lattice, with a ~25 % change in the {10-12} twinning shear accompanying the observed transition, while the as-cast morphology modulates the magnitude of the work-hardening response.*
4. This study provides fundamental insights into the Ti-Zr-Hf HEA system, establishing a clear composition-microstructure-property relationship. Future work should focus on two key directions to further unlock the potential of this system. First, precise compositional optimization within the single-phase HCP region — particularly fine-tuning the Ti/Zr/Hf ratio — offers a promising route to systematically modulate the stacking fault energy and thereby tailor the twinning propensity and TWIP response. Second, post-processing via thermomechanical treatment, such as cold rolling followed by controlled recrystallization annealing, provides a practical pathway to engineer well-defined grain sizes. Given that deformation twinning in HCP metals is strongly grain-size dependent — with coarser grains promoting twinning activation and finer grains suppressing it — grain size control through annealing represents a powerful lever for optimizing the strength-ductility balance, ultimately enabling the design of high-performance HCP HEAs tailored for targeted structural applications.

CRediT authorship contribution statement

Kooknoh Yoon: Writing – original draft, Visualization, Software, Methodology. **Haomin Lyu:** Writing – original draft, Visualization, Methodology. **Xiaoyu Chen:** Visualization, Methodology. **Andrew M. Minor:** Writing – review & editing, Validation, Supervision, Conceptualization. **Mark Asta:** Writing – review & editing, Supervision, Conceptualization. **Daryl Chrzan:** Writing – review & editing, Supervision, Project administration, Funding acquisition, Conceptualization. **Peter Hosemann:** Writing – review & editing, Validation, Funding acquisition, Conceptualization.

Declaration of competing interest

The authors declare that they have no known competing financial interests or personal relationships that could have appeared to influence the work reported in this paper.

We further declare that thi paper has not been submitted elsewhere.

Acknowledgement

This research was supported by the US National Science Foundation through the Division of Materials Research DMREF program award 2324022 and the research fund of Hanbat National University in 2026.

Additionally, we would like to express our sincere gratitude to Professor Eun Soo Park of the Department of Materials Science and Engineering at Seoul National University for his invaluable advice and assistance with the CALPHAD simulation during the alloy design process. Work at the Molecular Foundry was supported by the Office of Science, Office of Basic Energy Sciences, of the U.S. Department of Energy under Contract No. DE-AC02-05CH11231, under user proposal numbers MFP-9242 and MFP-10135.

Supplementary materials

Supplementary material associated with this article can be found, in the online version, at doi:10.1016/j.actamat.2026.122719.

References

[1] J.C. Williams, R.G. Baggerly, N.E. Paton, Deformation behavior of HCP Ti-Al alloy single crystals, Metall. Mater. Trans. A 33 (3) (2002) 837–850.
[2] C.H. Woo, Defect accumulation behaviour in hcp metals and alloys, J. Nucl. Mater. 276 (1-3) (2000) 90–103.
[3] D. Jany, E. Rothchild, D.C. Chrzan, Polymorphic structure of⟨ a⟩-type screw dislocation cores in α-Ti, Phys. Rev. Mater. 7 (10) (2023) 103603.
[4] M.H. Yoo, J.K. Lee, Deformation twinning in hcp metals and alloys, Philos. Mag. A 63 (5) (1991) 987–1000.
[5] H. Wang, P.D. Wu, J. Wang, C.N. Tomé, A crystal plasticity model for hexagonal close packed (HCP) crystals including twinning and de-twinning mechanisms, Int. J. Plast. 49 (2013) 36–52.
[6] K. Yao, X. Min, Static and dynamic Hall–Petch relations in {332}< 113>TWIP Ti–15Mo alloy, Mater. Sci. Eng. A 827 (2021) 142044.
[7] S. Zhao, R. Zhang, Q. Yu, J. El, R.O. Ritchie, A.M. Minor, Cryo-forged nanotwinned titanium with ultrahigh strength and ductility, Science 373 (6561) (2021) 1363–1368.
[8] Q. Yu, L. Qi, K. Chen, R.K. Mishra, J. Li, A.M. Minor, The nanostructured origin of deformation twinning, Nano Lett. 12 (2012) 887–892.
[9] V.V. Skripnyak, V.A. Skripnyak, Hexagonal close-packed (hcp) alloys under dynamic impacts, J. Appl. Phys. 131 (16) (2022).
[10] M. Reytier, F. Kircher, B. Levesy, Characterization of titanium alloys for cryogenic applications, in: AIP Conference Proceedings 614, American Institute of Physics, 2002, May, pp. 76–83.
[11] E.P. George, D. Raabe, R.O. Ritchie, High-entropy alloys, Nat. Rev. Mater. 4 (8) (2019) 515–534.

[12] ... & S. Zhao, S. Yin, X. Liang, F. Cao, Q. Yu, R. Zhang, A.M. Minor, Deformation and failure of the CrCoNi medium-entropy alloy subjected to extreme shock loading, Sci. Adv. 9 (18) (2023) eadf8602.
[13] H.S. Oh, D. Ma, G.P. Leyson, B. Grabowski, E.S. Park, F. Körmann, D. Raabe, Lattice distortions in the FeCoNiCrMn high entropy alloy studied by theory and experiment, Entropy 18 (9) (2016) 321.
[14] ... & H.S. Oh, K. Odbadrakh, Y. Ikeda, S. Mu, F. Körmann, C.J. Sun, E.S. Park, Element-resolved local lattice distortion in complex concentrated alloys: an observable signature of electronic effects, Acta Mater. 216 (2021) 117135.
[15] ... & S.S. Sohn, A. Kwiatkowski da Silva, Y. Ikeda, F. Körmann, W. Lu, W.S. Choi, D. Raabe, Ultrastrong medium-entropy single-phase alloys designed via severe lattice distortion, Adv. Mater. 31 (8) (2019) 1807142.
[16] B. Cantor, Multicomponent high-entropy Cantor alloys, Prog. Mater. Sci. 120 (2021) 100754.
[17] O.N. Senkov, G.B. Wilks, D.B. Miracle, C.P. Chuang, P.K. Liaw, Refractory high-entropy alloys, Intermetallics 18 (9) (2010) 1758–1765.
[18] J. Yang, Y.H. Jo, W. An, H.S. Kim, B.J. Lee, S. Lee, S.S. Sohn, Effects of deformation-induced martensitic transformation on cryogenic fracture toughness for metastable Si8V2Fe45Cr10Mn5Co30 high-entropy alloy, Acta Mater. 226 (2022) 117648.
[19] Y.H. Doh, K.Y. Kim, D.G. Lee, D.H. Kim, D.W. Sung, H.K. Sohn, S.S. Lee, D. Kim, H. S. Lee, B.J. Lee, Cryogenic-temperature fracture toughness analysis of non-equi-atomic V10Cr10Fe45Co20Ni15 high-entropy alloy, J. Alloys. Compd. 802 (2019) 502–512.
[20] X. Wang, D. Xu, W. Jiao, R. Huang, X. Du, P.K. Liaw, Y. Lu, Quantitative analysis of phase structures in classical high-entropy alloys with deep insights into deformation mechanisms, Mater. Sci. Eng. A 949 (2025) 149435.
[21] M.C. Gao, et al., High-entropy alloys in hexagonal close-packed structure, Metall. Mater. Trans. A 47 (7) (2016) 3322–3332.
[22] ... & C.L. Tracy, S. Park, D.R. Rittman, S.J. Zinkle, H. Bei, M. Lang, W.L. Mao, High pressure synthesis of a hexagonal close-packed phase of the high-entropy alloy CrMnFeCoNi, Nat. Commun. 8 (1) (2017) 15634.
[23] ... & J.W. Qiao, M.L. Bao, Y.J. Zhao, H.J. Yang, Y.C. Wu, Y. Zhang, M.C. Gao, Rare-earth high entropy alloys with hexagonal close-packed structure, J. Appl. Phys. 124 (19) (2018).
[24] Y.J. Zhao, J.W. Qiao, S.G. Ma, M.C. Gao, H.J. Yang, M.W. Chen, Y. Zhang, A hexagonal close-packed high-entropy alloy: The effect of entropy, Mater. Des. 96 (2016) 10–15.
[25] Z. Wang, M.L. Bao, X.J. Wang, P.K. Liaw, R.P. Guo, J.W. Qiao, Deformation mechanisms in hexagonal close-packed high-entropy alloys, J. Appl. Phys. 129 (17) (2021) 175104.
[26] W.J. Carpenter, Y. Yang, B. Gludovatz, W.A. Curtin, E.P. George, Effects of HCP/BCC element ratios on the room-temperature tensile properties of Ti-Zr-Hf-Nb-Ta refractory high-entropy alloys, Intermetallics 185 (2025) 108923.
[27] J. Ding, J. Gao, E. Zhang, Y. Tang, L. Zhang, X. Xia, Thermodynamic Modeling of the Ti-Hf-Zr-Nb-Ta Refractory High Entropy Alloy and Its Application in Analyzing Phase Stability, Comput. Mater. Contin. 85 (1) (2025).
[28] X. Wang, T. Li, D. Xu, Y. Wu, W. Jiao, P.K. Liaw, Y. Lu, Enabling high strength yet ductility in a refractory high-entropy alloy through oxygen-nitrogen synergistic effect, Acta Mater. 296 (2025) 121229.
[29] M. He, Y. Liu, Structural, electronic, and mechanical properties of Mg–Dy intermetallic compounds: a first-principles study, J. Magnes Alloys 12 (3) (2024) 415–426.
[30] J. Jeong, S.J. Kim, S.H. Park, Transmission electron microscopy and thermodynamic analysis on solubility limits of alloying elements in AZ31 magnesium alloys, Mater. Sci. Eng. A 564 (2013) 232–239.
[31] Z.L. Ning, W.Y. Sun, C.S. Xu, J.M. Hu, J. Meng, Microstructure and elevated temperature mechanical and creep properties of magnesium alloy WE43, Surf. Coat. Technol. 258 (2014) 1229–1235.
[32] W. Petry, A. Heiming, J. Trampenau, M. Alba, First-principles calculations on the bcc–hcp transition of titanium, Acta Mater. 48 (4) (2000) 1235–1245.
[33] Z. Hu, Y. Wang, The role of mechanical loading in bcc–hcp phase transition of titanium alloys, Acta Mater. 237 (2022) 118079.
[34] L. Wang, H. Yu, J. Zhang, Design strategy of Ti–Zr–Hf–Nb high-entropy alloys based on first-principles computations, J. Alloys. Compd. 968 (2025) 175642.
[35] A. Goryachev, V. Pastukhov, The melting diagram of the Ti-corner of the Ti–Zr–Si system and mechanical properties of as-cast compositions, J. Alloys. Compd. 366 (1–2) (2004) 142–149.
[36] T. Nagase, Y. Iijima, A. Matsugaki, K. Ameyama, T. Nakano, Design and fabrication of Ti–Zr–Hf–Cr–Mo and Ti–Zr–Hf–Co–Cr–Mo high-entropy alloys as metallic biomaterials, Mater. Sci. Eng. C 104 (2019) 109947.
[37] S. Jiang, Z. Xu, B. Wu, P. Mao, X. Du, Effects of atomic radius mismatch and Burgers vector magnitude on the tensile properties of Ti–Zr–V–Nb–Cr medium-entropy alloys, J. Alloys. Compd. 984 (2025) 173552.
[38] D. Ma, B. Grabowski, J. Neugebauer, Solid-solution strengthening in refractory high-entropy alloys, Acta Mater. 175 (2019) 239–249.
[39] K.H. Kumar, P. Wollants, L. Delacy, Thermodynamic assessment of the Ti-Zr system and calculation of the Nb-Ti-Zr phase diagram, J. Alloys. Compd. 206 (1) (1994) 121–127.
[40] J.P. Abriata, J.C. Bolcich, H.A. Peretti, The Hf− Zr (hafnium− zirconium) system, J. Ph Equilibria 3 (1) (1982) 29–34.
[41] J.L. Murray, The Hf− Ti (Hafnium-Titanium) system, Bull. Alloy Ph Diagr. 2 (2) (1981) 181–185.
[42] T. Li, S. Wang, W. Fan, Y. Lu, T. Wang, T. Li, P.K. Liaw, CALPHAD-aided design for superior thermal stability and mechanical behavior in a TiZrHfNb refractory high-entropy alloy, Acta Mater. 246 (2023) 118728.
[43] Ti, R.R.S.S.T., & Zr, V.Z. TCHEA3: TCS High Entropy Alloy Database.
[44] O.B. Perevalova, M.S. Syrtanov, In situ study of phase transformations in electron beam additive manufactured Ti-6Al-4 V titanium alloy by high temperature synchrotron X-ray diffraction and TEM, J. Alloys. Compd. 917 (2022) 165463.
[45] H. Beladi, Q. Chao, G.S. Rohrer, Variant selection and intervariant crystallographic planes distribution in martensite in a Ti–6Al–4V alloy, Acta Mater. 80 (2014) 478–489.
[46] M.A. Kumar, M. Wroński, R.J. McCabe, L. Capolungo, K. Wierzbanowski, C. N. Tomé, Role of microstructure on twin nucleation and growth in HCP titanium: A statistical study, Acta Mater. 148 (2018) 123–132.
[47] K.N. Yoon, H.S. Oh, J.Y. Kim, M.S. Kim, J. Zhang, E.S. Park, A new class of light-weight metastable high entropy alloy with high strength and large ductility, Materialia 21 (2022) 101284.
[48] C. Du, R. Petrov, M.G. Geers, J.P. Hoefnagels, Lath martensite plasticity enabled by apparent sliding of substructure boundaries, Mater. Des. 172 (2019) 107646.
[49] J.H. Jung, A. Forslund, P. Srinivasan, B. Grabowski, Dynamically stabilized phases with full ab initio accuracy: Thermodynamics of Ti, Zr, Hf with a focus on the hcp-bcc transition, Phys. Rev. B 108 (18) (2023) 184107.
[50] Y. Kuang, Generation of TTT and CCT curves for cast Ti-6Al-4V alloy. Doctoral dissertation, University of Florida, 2004.
[51] H. Kawata, Y. Honda, K. Nakano, K. Takeda, K. Hikida, Strengthening via grain refinement in lath martensite on low carbon Fe–18Ni alloys, ISIJ Int. 62 (7) (2022) 1502–1511.
[52] I. Basu, J.T.M. De Hosson, Strengthening mechanisms in high entropy alloys: fundamental issues, Scr. Mater. 187 (2020) 148–156.
[53] D. Tabor, The hardness of metals, Oxford university press, 2000.
[54] ... & S. Wang, D. Shu, P. Shi, X. Zhang, B. Mao, D. Wang, B. Sun, TiZrHfNb refractory high-entropy alloys with twinning-induced plasticity, J. Mater. Sci. Technol. 187 (2024) 72–85.
[55] M.H. Yoo, Slip, twinning, and fracture in hexagonal close-packed metals, Metall. Trans. A 12 (3) (1981) 409–418.
[56] M.H. Yoo, J.R. Morris, K.M. Ho, S.R. Agnew, Nonbasal deformation modes of HCP metals and alloys: Role of dislocation source and mobility, Metall. Mater. Trans. A 33 (3) (2002) 813–822.
[57] P. Agrawal, S. Gupta, S. Thapliyal, S. Shukla, R.S. Haridas, R.S. Mishra, On the evolving nature of c/a ratio in a hexagonal close-packed epsilon martensite phase in transformative high entropy alloys, Sci. Rep. 9 (2019) 13608.
[58] S. Chen, K.K. Tseng, Y. Tong, W. Li, C.W. Tsai, J.W. Yeh, P.K. Liaw, Grain growth and Hall-Petch relationship in a refractory HfNbTaZrTi high-entropy alloy, J. Alloys. Compd. 795 (2019) 19–26.